Nonthermal Synthesis of Three-Dimensional Metal Oxide Structures under Continuous-Flow Conditions and Their Catalytic Applications

9 AUTHORS, INCLUDING:

Naftali Opembe
Ames Laboratory of the US DOE
17 PUBLICATIONS **276** CITATIONS

SEE PROFILE

Aparna Iyer
University of Connecticut
7 PUBLICATIONS **157** CITATIONS

SEE PROFILE

Hui Huang
University of Connecticut
22 PUBLICATIONS **804** CITATIONS

SEE PROFILE

Steven L Suib
University of Connecticut
**652** PUBLICATIONS **15,529** CITATIONS

SEE PROFILE

Nonthermal Synthesis of Three-Dimensional Metal Oxide Structures under Continuous-Flow Conditions and Their Catalytic Applications

Cecil K. King'ondu,[†] Naftali N. Opembe,[†] Homer C. Genuino,[†] Hector F. Garces,[‡]
Eric C. Njagi,[†] Aparna Iyer,[†] Hui Huang,[†] Saminda Dharmarathna,[†] and Steven L. Suib*,[†,‡]

[†]Department of Chemistry and [‡]Institute of Materials Science, University of Connecticut, Storrs, Connecticut 06269, United States

S *Supporting Information*

ABSTRACT: Continuous-flow synthesis of one-dimensional (1D) metal oxide nanostructures and/or their integration into hierarchical structures under nonthermal conditions is still a challenge. In this work, a nonthermal, continuous-flow approach for the preparation of γ-manganese oxide (γ-MnO$_2$) and cerium oxide (CeO$_2$) microspheres has been developed. By this technique, γ-MnO$_2$ materials with surface areas of 240, 98, and 87 m^2/g and CeO$_2$ microspheres with a surface area of 1 m^2/g have been fabricated successfully. Characterization of the materials was carried out using powder X-ray diffraction, infrared and inductively coupled plasma optical emission spectrometer (ICP/OES), nitrogen sorption, scanning electron microscopy, transmission electron microscopy, and thermogravimetric analysis. The synthesized materials showed good catalytic activity in the oxidation of α-methyl styrene.
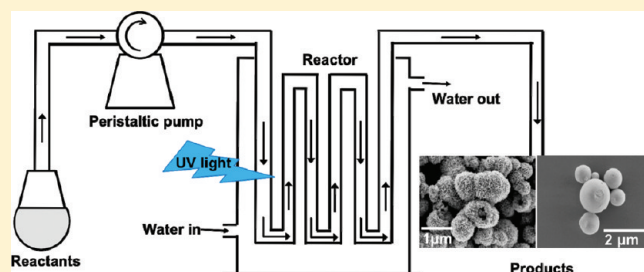
■ INTRODUCTION

Mixed-valence, tunnel structures and lattice defects, such as oxygen vacancies, have been reported to confer unique electronic, magnetic, physical, or chemical properties to nanomaterials.[1] As a result, metal oxides that inherently possess these features, for instance, γ-manganese oxide (γ-MnO$_2$), cryptomelane-type manganese oxide octahedral molecular sieves (OMS-2), and cerium oxide (CeO$_2$) materials, have lately been the subject of considerable research interest due to their current and/or anticipated applications.

CeO$_2$ materials are presently being used in automobiles, cosmetics, electronics, and fuel cell industries to make three-way exhaust catalysts,[2] sunscreen,[3,4] dielectric materials,[5] and solid electrolytes.[6] This is due to a reversible Ce^{3+}/Ce^{4+} redox couple, a high dielectric constant, a strong ligand-to-metal charge-transfer absorption band in the ultraviolet region (210–310 nm),[7] and oxygen vacancies in these materials. On the other hand, γ-MnO$_2$ materials find applications in the battery industry as cathode materials[8] and as catalysts to transform organic molecules into more useful intermediates or final products.[9] Recently, Jin et al.[10] converted toluene to benzoic acid and benzylaldehyde using γ-MnO$_2$ as a catalyst. The activity of the γ-MnO$_2$ materials in energy storage and catalytic transformations is suggested to arise from their innate de Wolff phase changes, microtwinning, and point defects.[11] Moreover, the mixed valency and tunnel structure of the OMS-2 materials make them effective catalysts for mild, but highly selective, oxidation of alcohols to aldehydes and ketones,[12] synthesis of new organic compounds,[13] decomposition of organic pollutants,[14] and effective molecular sieves for the separation of heavy metal ions.[15]

Because of the above-mentioned applications, current and/or anticipated, a number of strategies have been developed to synthesize γ-MnO$_2$, OMS-2, and CeO$_2$ materials and to adapt their particle sizes and morphologies. Most of these strategies that have been reported entail wet-chemical reactions carried out under hydrothermal or reflux conditions in a batch mode. As such, thermal energy provided by an oil bath or microwave radiation is often used.[16] CeO$_2$ nanostructures have been synthesized through calcination of a CeCO$_3$OH precursor prepared under batch hydrothermal conditions.[17] In addition to thermal methods, room-temperature synthesis of γ-MnO$_2$ has been reported.[18] However, this batch technique involves two steps and long reaction times (about 12 h). Moreover, King'ondu et al.[19] recently prepared γ-MnO$_2$, CeO$_2$, and CoOOH materials by UV light irradiation, albeit in a batch mode.

To circumvent the problems associated with batch reactors, such as time consumption during precursor(s) charging and product(s) discharge, tubular reactors have been developed to perform multikilogram, continuous-flow synthesis of metal oxide nanomaterials. ZnO, AlOOH, CuO, Fe$_2$O$_3$, TiO$_2$, and CeO2 materials have thus been prepared under continuous-flow conditions using supercritical water and/or methanol.[20] Recently, Opembe et al.[21] synthesized manganese oxide (OMS-2) under microwave-assisted continuous-flow conditions. In this case, organic additive(s), for instance, dimethyl sulfoxide (DMSO), was used to promote superheating of the

reactant mixture, thereby realizing continuous-flow synthesis of OMS-2.

While the current continuous mode methods have increased the scale of the metal oxide material synthesis and thus remedied the problems associated with batch reactors, such as multiple steps, a trade-off between short reaction times and the cost of reactor, imposed by the use of high temperatures and pressures, is almost inevitable with these strategies. The use of organic additives, as is the case in Opembe et al.'s[21] work, is also an additional cost. Herein, we report the continuous-flow syntheses of CeO_2, γ-MnO_2, and OMS-2 materials under nonthermal and atmospheric (pressure) conditions. The method is based on the use of ultraviolet (UV) light to effect rapid decomposition of persulfate ions ($S_2O_8{}^{2-}$) into highly oxidizing photoproducts, sulfate radicals ($SO_4{}^{\bullet-}$). The $SO_4{}^{\bullet-}$ generated then oxidizes Mn^{2+} and Ce^{3+} ions in the reaction media to their respective γ-MnO_2, OMS-2, and CeO_2 oxides. UV light has extensively been used in continuous-flow degradation of dyes and other organic compounds.[22] However, synthesis of metal oxide hierarchical structures under continuous-flow conditions using UV light has not been reported.

■ EXPERIMENTAL METHODS

Materials. Manganese(II) sulfate monohydrate ($MnSO_4 \cdot H_2O$), potassium persulfate ($K_2S_2O_8$), potassium sulfate (K_2SO_4), cerium(III) nitrate hexahydrate ($Ce(NO_3)_3 \cdot 6H_2O$), α-methyl styrene, acetonitrile (ACN), dimethylformamide (DMF), and tert-butyl hydroperoxide (70% in water, TBHP) were purchased from Sigma-Aldrich, whereas concentrated nitric (HNO_3) and sulfuric (H_2SO_4) acids were both obtained from Alfa Aesar. All reagents were used without any further purification.

Photoreactor Setup. Continuous-flow syntheses were conducted in a Rayonet RPR-1092 photoreactor (The Southern New England Ultraviolet Co.); see the Supporting Information, Figure S1, for pictorial details. The photoreactor is equipped with 12 low-pressure mercury lamps with a peak spectral energy distribution at 253.7 nm. The system has a fan cooling system, but in our syntheses, a coiled tubular quartz reactor was jacketed with flowing water to eliminate thermal (infrared) effects. The dimensions of the tubular quartz reactor were Φ_{inner} = 1/8 in., Φ_{outer} = 1/4 in., and L = 48 in. The coiled reactor was continuously charged with clear precursor solutions by use of a peristaltic pump (operated from outside the photoreactor) connected to the coiled tubular reactor inlet on one end and to the precursor solution reservoir on the other end. The peristaltic pump served to control the flow rates. Effects of flow rates, type of acid, wavelength, and UV intensity on the morphology and cystallinity of the products were investigated. Microwave heating—for comparison with UV light irradiation—was conducted in a CEM Mars 5 multimode microwave equipped with one magnetron, a fixed frequency of 2.45 GHz, and a three-level power output of 300, 600, and 1200 W. In this study, only a 300 W power output was used.

Synthesis. In a typical synthesis of γ-MnO_2, 1.35 g (7.98 mmol) of $MnSO_4 \cdot H_2O$ and 3.25 g (12.0 mmol) of $K_2S_2O_8$ were added to 200 mL of distilled—deionized water (DDW) containing 3 mL of concentrated HNO_3 or concentrated H_2SO_4 and then stirred to make a clear solution. To synthesize CeO_2 materials, the above-mentioned procedure remained the same except that 1.35 g (3.1 mmol) of $Ce(NO_3)_3 \cdot 6H_2O$ was used in place of $MnSO_4 \cdot H_2O$. To synthesize OMS-2, 1.35 g (7.98 mmol) of

$MnSO_4 \cdot H_2O$, 2.10 g (12.1 mmol) of K_2SO_4, and 3.25 g (12.0 mmol) of $K_2S_2O_8$ were added to 200 mL of DDW containing 3 mL of concentrated nitric acid and then stirred to make a clear solution. Rubber tubing was then connected to the flask containing the clear precursor solution, through a peristaltic pump to the inlet of the coiled quartz reactor maintained in the UV light cavity. Because no precipitate was formed when γ-MnO_2, OMS-2, and CeO_2 precursors were dissolved in distilled water, the resultant precursor solutions were continuously charged without stirring, through a coiled quartz reactor at different flow rates, where they interacted with ultraviolet light for a given duration of time. Subsequently, the products were collected at the discharge end of the reactor, centrifuged, washed with DDW, and dried at 120 °C overnight.

■ CHARACTERIZATION

Structural Study. Structural studies were done by X-ray powder diffraction (XRD) analysis performed on a Scintag XDS-2000 diffractometer with Cu Kα radiation (λ = 0.15406 nm) operating at a current of 40 mA and a beam voltage of 45 kV. The powdered samples were loaded on a glass sample holder and the patterns collected continuously at a scan rate of 2.0 °/min. Further structural studies were done using high-resolution transmission electron microscopy (HRTEM) with a JEOL JEM 2010 FasTEM operating at 200 kV. The samples for the TEM were prepared by dispersing the powdered materials in ethanol. The suspension was then sonicated for 3—5 min, and a drop of solution was loaded on a carbon-coated copper grid and dried before analysis.

Morphology and Elemental Studies. The morphology of the products was studied by field emission scanning electron microscopy (FESEM) using a Zeiss DSM 982 Gemini instrument equipped with a Schottky emitter at an accelerating voltage of 2.0 kV and a beam current of 1.0 mA. The FESEM samples were prepared by dispersing the powdered samples in absolute ethanol. The suspension was then sonicated for 3—5 min, and a drop was loaded on Au—Pd-coated silicon glass chips mounted onto aluminum stubs with a two-sided carbon tape. Prior to SEM analysis, the samples were dried by vacuum desiccation. Elemental analyses, particularly sulfur content determinations, were done at the Center for Environmental Sciences and Engineering, using a PerkinElmer 7300DV Dual View inductively coupled plasma optical emission spectrometer (ICP/OES) according to established protocols. In summary, the samples were homogenized and approximately 0.02 g of each sample was placed into hot block tubes. A 25 mL portion of concentrated trace metal grade nitric acid was then added to each tube and placed in the hot block and refluxed for 4 h at 95 °C. The samples were cooled, 2 mL of distilled (DI) water and 3 mL of trace metal grade hydrogen peroxide were added, and the samples were heated in the hot block until the effervescence subsided. The samples were once again cooled and brought to a final volume of 50 mL with DI water. All samples were analyzed at either 10× or 40× dilutions due to interferences with the analysis. Standard quality assurance procedures were employed, including analysis of initial and continuing calibration checks and blanks, duplicate samples, preparation blanks (Blank), post digestion spiked samples, and laboratory control samples (LCS). All results were within the established quality control parameters.

Surface Area and Pore Size Distribution. Surface area and porosity studies were done on a Micrometrics ASAP 2010

23274

dx.doi.org/10.1021/jp206942u |J. Phys. Chem. C 2011, 115, 23273–23282

accelerated surface area system. N_2 gas was used as the adsorbate at 77 K, and the samples were degassed at 150 °C for 12 h prior to the sorption studies. The specific surface area of the material was calculated using the Brunauer—Emmett—Teller (BET) method while the pore size distribution was determined using Barrett—Joyner—Halenda (BJH) methods.

Fourier Transform Infrared (FTIR) Spectroscopy and Thermal Stability Studies. To study the surface and functional group properties of the prepared materials, Fourier transform infrared (FTIR) spectra were obtained at room temperature using a Nicolet Magna-IR system 560 FTIR spectrometer with a DTGS detector. The powdered specimens were first diluted with KBr at a ratio of 1:100 and then pressed into a pellet. The spectral background was collected using pure KBr discs. Thermogravimetric analysis (TGA) and differential scanning calorimetry (DSC) were performed in a Hi-Res TA Instruments model 2950 and a DSC model Q20, respectively. In both TGA and DSC experiments, the temperature ramp rate was 20 °/min in a nitrogen atmosphere.

Catalytic Applications. The catalytic activity of the synthesized γ-MnO_2 and OMS-2 materials was examined in the oxidation of α-methyl styrene using tertiary butyl hydroperoxide (TBHP) as an oxidant. The catalytic oxidation reactions were carried out in a round-bottom flask. Prior to catalytic studies, 50 mg of γ-MnO_2 catalysts was dried at 120 °C for 6 h, then added separately to two 50 mL, two-neck round-bottom flasks containing 1.0 mmol of α-methyl styrene and 2.0 mmol of TBHP in 10.0 mL of 9:1 acetonitrile/dimethylformamide (ACN/DMF). The reaction mixture was then refluxed at 80 °C for 4 h in an oil bath and the products filtered and analyzed. Qualitative and quantitative analyses of the reaction products was done using a 5890 Series II gas chromatograph connected to an HP 5971 mass selective detector through an HP-1 nonpolar cross-linked methyl siloxane column with dimensions of 12.5 m × 0.2 mm × 0.33 μm.

RESULTS

Comparison between Microwave and UV-Light-Assisted Generation of the Sulfate Radicals. Because superheating is attainable in microwave-promoted syntheses[21,23] and thermal heating has been reported to facilitate the decay of $S_2O_8^{2-}$ ions,[24] we sought to investigate how microwave-assisted decomposition of $S_2O_8^{2-}$ ions and consequent generation of sulfate radicals (which are the basis of our strategy) compare with the UV-light-promoted procedure. To do this, 5.0 mL/min was chosen as the representative flow rate and a clear γ-MnO_2 precursor solution was charged through the coiled quartz reactor illuminated with 12 low-pressure mercury lamps (λ = 253.7 nm). After this, another batch of clear γ-MnO_2 precursor solution was charged at the same flow rate (5.0 mL/min) through a CEM Mars 5 multimode microwave oven equipped with the same quartz reactor used in the photolysis; see the Supporting Information, Figure S1, for microwave pictorial details. When UV light was used, a dark brown suspension was collected at the discharge end of the quartz reactor. In marked contrast, when microwave heating was used, the clear γ-MnO_2 precursor solution passed through the microwave cavity unaffected (in terms of color), albeit attaining a temperature of about 80 °C, and a clear γ-MnO_2 precursor solution was collected at the discharge end; see the Supporting Information, Figure S2a.
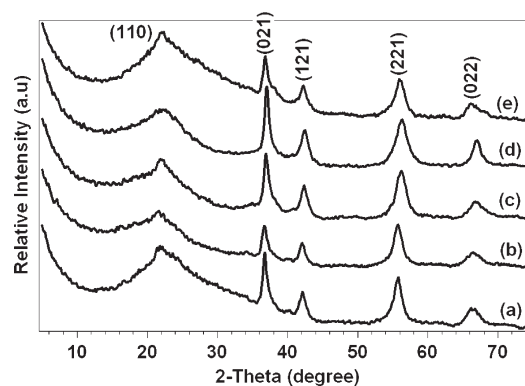

Figure 1. XRD patterns of γ-MnO_2 prepared with nitric acid at (a) 1.0, (b) 2.0, (c) 4.0, and (d) 7.0 mL/min, and (e) at 2.0 mL/min without acid.
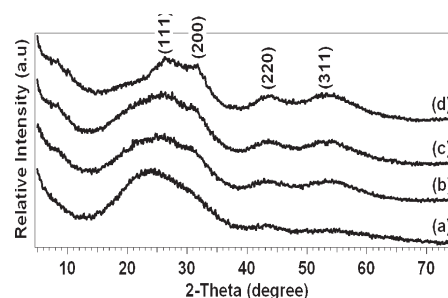

Figure 2. XRD patterns of CeO_2 prepared with nitric acid at (a) 7.0, (b) 4.0, (c) 2.0, and (d) 1.0 mL/min.

Effects of Flow Rates on the Phase Evolution and Crystallinity. To study the effects of flow rates on the crystallinity and morphology of the γ-MnO_2, OMS-2, and CeO_2 materials, 12 low-pressure mercury lamps with 253.7 nm (wavelength) and nitric acid were used. The flow rates were then varied in the following manner: 1.0, 2.0, 4.0, and 7.0 mL/min for all the materials. As shown by the XRD patterns in Figure 1, crystalline γ-MnO_2 materials were obtained at all the flow rates used. No significant change in crystallinity with the flow rate was observed. The diffraction peaks (Figure 1) observed for these materials could be indexed to the γ-manganese oxide, consistent with the work of Yuan et al.[18] To ascertain whether the crystalline phase of the as-synthesized γ-MnO_2 evolved during the nonthermal UV irradiation stage or during the drying stage, γ-MnO_2 was synthesized at 2.0 mL/min, filtered, washed, and dried at room temperature. The XRD pattern of this sample did not show any significant change in peak broadness or intensities when compared to a sample prepared under the same conditions but dried at 120 °C overnight; see the Supporting Information, Figure S3.

Cerium oxide materials synthesized at 1.0, 2.0, 4.0, and 7.0 mL/min (Figure 2) showed broad XRD peaks that could be indexed to the face-centered cubic structure of CeO_2, based on the Joint Committee on Powder Diffraction Standards [JCPDS] Card No. 78-0694. Unlike γ-MnO_2 materials, which did not show any obvious change in peak intensity and broadness with flow rates, CeO_2 materials synthesized at the lowest flow rate (1.0 mL/min) showed relatively high peak intensities (Figure 2, pattern d) as compared with those prepared at higher flow rates (Figure 2, patterns a—c).
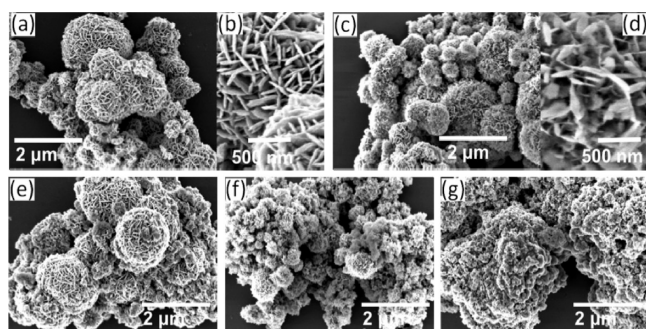
Figure 3. FESEM images of γ-MnO$_2$ prepared with nitric acid: (a) 1.0 mL/min, (b) high magnification of (a), (c) 2.0 mL/min, (d) high magnification of (c), (e) 4.0 mL/min, and (f) 7.0 mL/min. (g) 2.0 mL/min without acid.
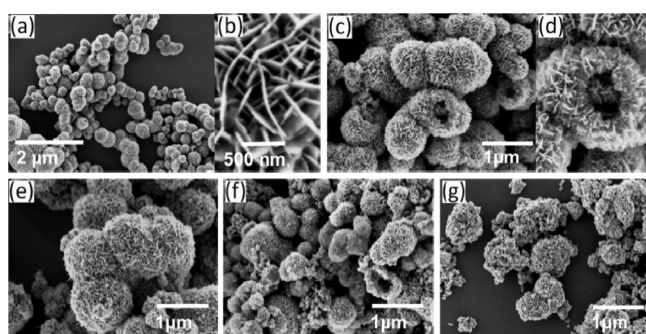

Figure 4. FESEM images of γ-MnO$_2$ prepared with sulfuric acid: (a) general morphology at 1.0 mL/min, (b) high magnification of (a), (c) 1.0 mL/min, (d) high magnification of (c), (e) 2.0 mL/min, (f) 4.0 mL/min, and (g) 7.0 mL/min.

Figure 5. FESEM images of CeO$_2$ prepared with nitric acid: (a) general morphology at 1.0 mL/min, (b) isolated CeO$_2$ microspheres, (c) 2.0 mL/min, (d) 4.0 mL/min, and (e) 7.0 mL/min. (f) 1.0 mL/min without acid.

In contrast to CeO$_2$ and γ-MnO$_2$ materials, flow rates had a more profound effect on the crystallization and formation of the OMS-2 materials. Pure crystalline phase OMS-2 materials could not be obtained at all the flow rates regardless of the manipulation of the UV light intensity and the pH of the precursor solution. At the lowest flow rate (1.0 mL/min), materials containing a mixture of OMS-2 and γ-MnO$_2$ phases were obtained; see the Supporting Information, Figure S4, pattern a. Above 1.0 mL/min, no OMS-2 phase was observed; instead, crystalline γ-MnO$_2$ materials were exclusively formed (the Supporting Information, Figure S4, patterns b and c).

Effects of Type of Acid and Flow Rates on Morphology. Morphological studies performed by FESEM showed that flow rates and type of acid greatly influenced the morphology of the as-synthesized materials. At the lowest flow rate (1.0 mL/min), microspheres were obtained for γ-MnO$_2$ and CeO$_2$ materials (panel (a) of Figures 3−5, in that order). However, upon increasing the flow rate, the microsphere morphology of the γ-MnO$_2$ and CeO$_2$ materials diminished; see Figures 3f, 4g, and 5e. Likewise, OMS-2 microspheres were obtained at the lowest flow rate, albeit with impurities; see the Supporting Information, Figure S5. At the higher flow rates of 2.0, 4.0, and 7.0 mL/min, the microspheres observed (see the Supporting Information, Figure S6) were made up of γ-MnO$_2$ materials whose XRD pattern is shown in the Supporting Information, Figure S4, pattern b.

To investigate the effect of the type of acid on the morphology, 1.0 mL/min was chosen as the flow rate and the UV light intensity
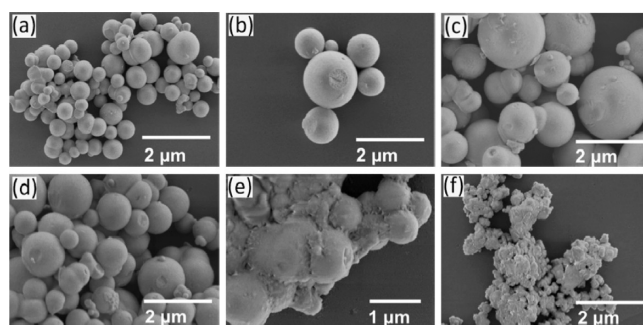
was kept constant by maintaining the same number of UV lamps. The γ-MnO$_2$ materials prepared with nitric acid showed countable microspheres (Figure 3a), whereas for their sulfuric acid counterparts, an homogeneous morphology predominantly consisting of well-formed microspheres was observed (Figure 4a). In addition, the core−shell morphology manifested by the sulfuric-acid-prepared γ-MnO$_2$ microspheres (Figure 4c,d) was not observed in the nitric-acid-prepared γ-MnO$_2$ materials. In the absence of either HNO$_3$ or H$_2$SO$_4$, however, no γ-MnO$_2$ microspheres were observed; instead, clusters of flakelike γ-MnO$_2$ particles were observed (Figure 3g).

The effects of the flow rate and type of acid on the morphology of the as-synthesized materials were more explicit for CeO$_2$ materials than for γ-MnO$_2$ materials. In the presence of HNO$_3$, well-formed CeO$_2$ microspheres were formed at the lowest flow rate (Figure 5a). This morphology was still observed at the relatively higher flow rates (2.0 and 4.0 mL/min, Figure 5c,d). However, at the highest flow rate (7.0 mL/min), poorly developed CeO$_2$ microspheres were obtained (Figure 5e).

Quite the opposite of the HNO$_3$ results, no solid CeO$_2$ products were obtained when H$_2$SO$_4$ was used. Instead, the clear CeO$_2$ precursor solution (containing H$_2$SO$_4$) turned yellow on passing through the UV light cavity and yellow solution was collected at the discharge end of the coiled reactor. Moreover, in the absence of both nitric and sulfuric acids, irregular CeO$_2$ clusters were obtained even at the lowest flow rate (1.0 mL/min, Figure 5f), as compared with well-formed microspheres obtained at the same flow rate, but in the presence of nitric acid (Figure 5a).

Effects of the pH and Sulfate Ion Concentration on Morphology. Because the absence and presence of and/or type of acid showed great influence on the morphology of γ-MnO$_2$ and CeO$_2$ materials (Figure 6a), the influence of pH on morphology was investigated. The effect of pH was studied by varying the amount of conc. HNO$_3$ added. Nitric acid was chosen instead of sulfuric acid to avoid SO$_4^{2-}$ ion contribution (if any) to the morphology. As shown in Figures 3a and 6a, aggregate clusters of γ-MnO$_2$ materials were obtained at pH 3.88, which is the pH of the reaction mixture in the absence of HNO$_3$. When the pH was lowered to 1.6, no γ-MnO$_2$ microspheres were observed. However, lowering the pH further gave pseudomicrospheres and well-developed γ-MnO$_2$ microspheres at pH 1.3 and 1.0, respectively. At a pH lower than 1.0, no substantial solid γ-MnO$_2$ products formed. Likewise, pH had a great influence on CeO$_2$ materials. In the absence of acid (pH 3.67), irregular CeO$_2$

23276

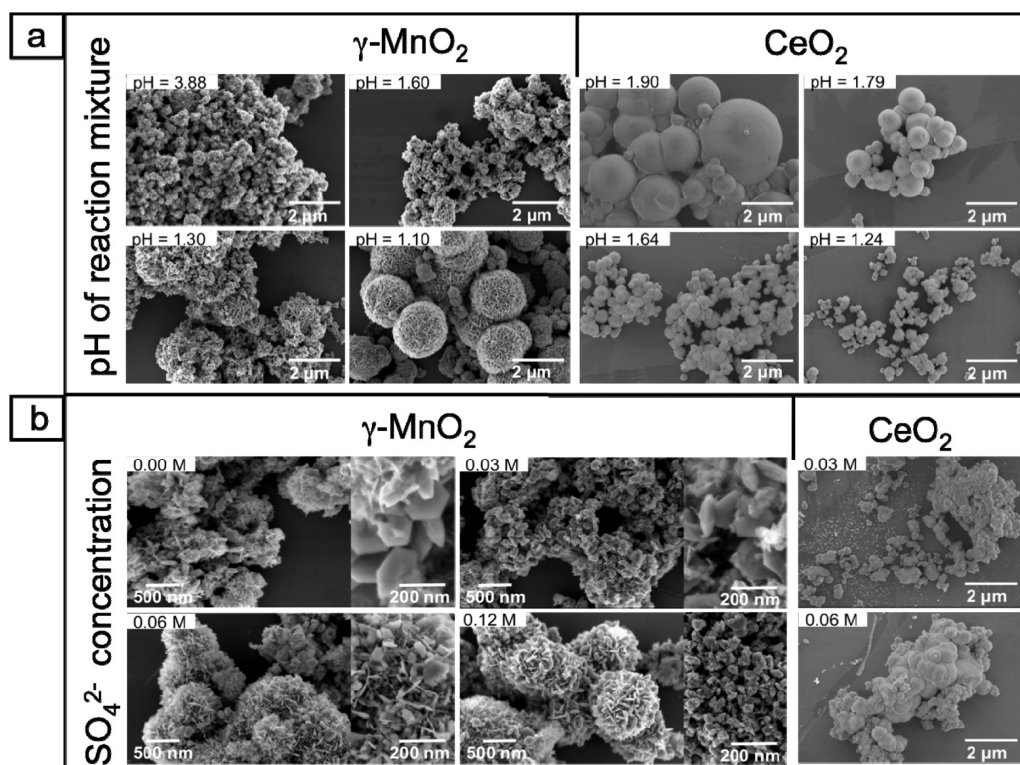dx.doi.org/10.1021/jp206942u |*J. Phys. Chem. C* 2011, 115, 23273–23282

Figure 6. FESEM images of γ-MnO$_2$ and CeO$_2$ prepared at (a) different pHs and (b) different sulfate concentrations. The images (at 200 nm magnification) on the right-hand γ-MnO$_2$ panel in (b) represents the size and shape of the particles constructing the γ-MnO$_2$ materials prepared at different SO$_4^{2-}$ concentrations.

clusters were obtained (Figure 5f). At pH 1.90, relatively large microspheres formed. Upon decreasing the pH to 1.79, 1.64, and 1.24, the sizes of the CeO$_2$ microsphere generally decreased (Figure 6a). However, at pH 1.18 and below, a yellow solution (instead of solid CeO$_2$ product) was obtained.

To study the effects of sulfate ion on the morphology of γ-MnO$_2$ materials, pH 1.6 was chosen (at this pH, no microspheres were obtained) and varying amounts of potassium sulfate (K$_2$SO$_4$) were introduced in the reaction mixture. The sulfate ion contribution from K$_2$S$_2$O$_8$ (oxidant) is constant and thus neglected in this study. At a SO$_4^{2-}$ ion concentration of 0.00 M (when no K$_2$SO$_4$ was added) and 0.03 M, aggregated clusters of γ-MnO$_2$ were obtained. However, when the concentration was increased to 0.06 and 0.12 M, poorly formed and well-developed γ-MnO$_2$ microspheres were obtained, respectively (Figure 6b). On the other hand, the SO$_4^{2-}$ ion effect on the morphology of CeO$_2$ materials was studied at pH 3.67 (pH at which no acid was added), since this was the pH at which no CeO$_2$ microspheres were observed. Unlike γ-MnO$_2$ materials, variation of the SO$_4^{2-}$ ion concentration from 0.00 to 0.06 M did not give an observable change in the morphology of CeO$_2$ materials (Figure 6b), while 0.12 M SO$_4^{2-}$ ions could not be attained due to the insolubility of K$_2$SO$_4$ in the CeO$_2$ precursor solution. See the Supporting Information for the flow rate used and the amounts of HNO$_3$ and K$_2$SO$_4$ used to attain the above-mentioned pH and SO$_4^{2-}$ ion concentrations, respectively.

Effects of the UV Light Intensity and Wavelength on Morphology. To ascertain the effects of wavelength on the morphology of the as-synthesized materials, nitric acid, γ-MnO$_2$, and 1.0 mL/min were chosen as the representative type of acid, material, and flow rate, respectively. The low-pressure mercury

lamps (λ = 253 nm) used to prepare γ-MnO$_2$ and CeO$_2$ materials shown in Figures 3–5, were replaced with an equal number of lamps having a wavelength of 350 or 700–400 nm; then a clear γ-MnO$_2$ precursor solution was charged through the coiled quartz reactor.

Upon replacing the 253 nm mercury lamps with 350 nm ones, a light brown product solution was collected at the discharge end of the reactor, in contrast to the dark brown suspension obtained with 253 nm lamps. The light brown solution did not give any meaningful γ-MnO$_2$ solid products (after centrifuging). In contrast to the 253 and 350 nm lamp results, the visible lamps (λ = 700–400 nm) had little or no effect on the clear γ-MnO$_2$ precursor solution; the precursor solution remained clear even after passing through the coiled quartz reactor illuminated with the visible light. See the Supporting Information, Figure S2b–d.

Transmission Electron Microscopy. More structural studies to confirm the impurities in the OMS-2 materials and to understand the internal organization of the obtained γ-MnO$_2$ and CeO$_2$ microspheres was done with high-resolution transmission electron microscopy (HRTEM). As shown in the HRTEM micrographs in Figure S7a (Supporting Information), the microspheres of the impure OMS-2 materials consisted of empty cores and porous shells. The porous shells are constructed of crystalline nanorods (Figure S7b, Supporting Information) with periodic lattice fringes of 4.8 Å that correspond to the interplanar spacing of (200) planes (Figure S7c, Supporting Information). In contrast to OMS-2, cerium oxide materials prepared at the same flow rate (1.0 mL/min) consisted of solid microspheres constructed from very small (1.1 nm) crystallites. This is in agreement with the XRD pattern of the CeO$_2$ material (Figure 2, pattern d) that shows broad peaks associated with small crystallites. The as-synthesized
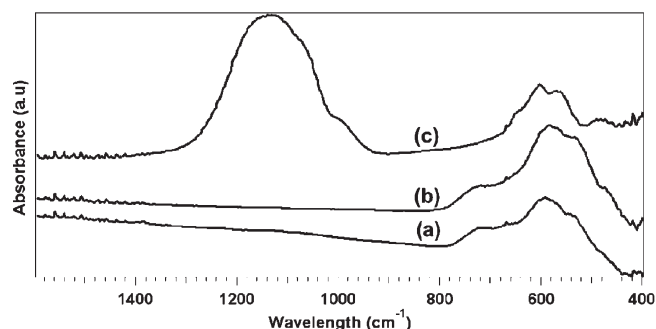
Figure 7. FTIR spectra of materials prepared at 1.0 mL/min: (a) γ-MnO_2 synthesized with nitric acid, (b) γ-MnO_2 synthesized with sulfuric acid, and (c) CeO_2 synthesized with nitric acid.

Table 1. Sulfur Content in Representative γ-MnO_2 and CeO_2 Materials Prepared at Different pHs

sample	pH[a]	sulfur content (mg/g)[b]
CeO_2	3.67	54.91(0.79)
CeO_2	1.90	57.23(0.42)
CeO_2	1.79	58.05(1.34)
CeO_2	1.64	57.93(1.16)
CeO_2	1.24	53.08(0.33)
γ-MnO_2	1.10	not detected

[a] pH values were measured using a pH meter (Fischer Scientific, Accumet pH Meter 25). [b] Sulfur content quantified by ICP-OES. Percent relative standard deviation given in parentheses.

γ-MnO_2 materials, on the other hand, are made up of crystalline nanofibers; see the Supporting Information, Figure S8.

Fourier Transform Infrared (FTIR) and Inductively Coupled Plasma Optical Emission Spectrometry (ICP-OES). The vibrational behavior of the lattice and surface species in γ-MnO_2 and CeO_2 materials was studied by FTIR spectroscopy. As shown in spectra a and b in Figure 7, the FTIR spectra of γ-MnO_2 materials show absorption bands between 800 and 400 cm^{-1} that are similar to those previously reported.[25] On the other hand, CeO_2 materials (Figure 7, spectrum c) show absorption peaks in the 700−400 cm^{-1} region and a broad band between 1250 and 950 cm^{-1} that is not observed in γ-MnO_2 materials.

Elemental analyses, particularly sulfur content determinations, in the representative γ-MnO_2 (prepared at pH 1.3 and a flow rate of 2.0 mL/min) and CeO_2 materials (prepared at 2.0 mL/min at varying pHs of 1.90, 1.79, 1.64, and 1.24) done by inductively coupled plasma optical emission spectrometry (ICP-OES) show no sulfur in the γ-MnO_2 samples. However, a substantial amount of sulfur (about 56.24 mg/g on average) was detected in CeO_2 materials prepared at different pHs even after washing several times with large amounts (2000 mL) of water. No significant change in the amount of sulfur with pH was observed; see Table 1.

Surface Area and Pore Distribution Studies. The N_2 adsorption/desorption isotherms, pore size distribution, and surface areas of the representative γ-MnO_2 and CeO_2 materials were acquired using a Micrometrics ASAP 2010 accelerated surface area system. The N_2 adsorption/desorption isotherms of the γ-MnO_2 samples (Figure 8) show fairly large hysteresis loops in the P/P_o range above 0.6, and a monotonic increase in the volume of adsorbed gas at relative pressures P/P_o greater than
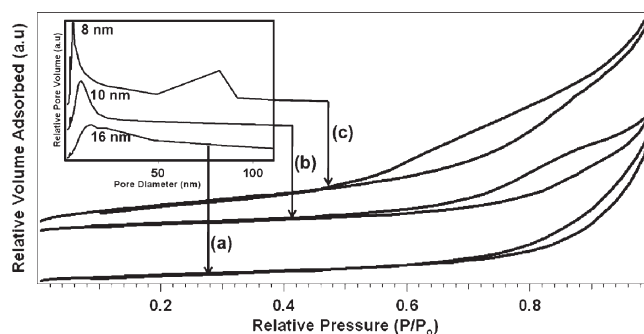

Figure 8. N_2 adsorption/desorption isotherms for γ-MnO_2 materials prepared with sulfuric acid at (a) 4.0, (b) 2.0, and (c) 1.0 mL/min. The inset shows pore size distributions calculated by the BJH method from the corresponding desorption branches.
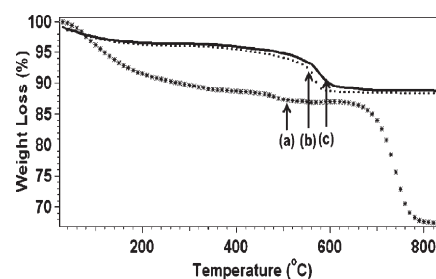

Figure 9. TGA profiles of materials prepared at 1.0 mL/min: (a) CeO_2 synthesized with nitric acid, (b) γ-MnO_2 synthesized with sulfuric acid, and (c) γ-MnO_2 synthesized with nitric acid.

0.75. These N_2 isotherms and their corresponding hysteresis loops (Figure 8) are similar to those in the literature.[11c,18,19,26] When the flow rate was increased, the size of the hysteresis loop decreased (Figure 8, curves a−c). Similarly, the BET surface areas of the γ-MnO_2 materials prepared with sulfuric acid decreased with an increase in flow rate. At flow rates of 1.0, 2.0, and 4.0 mL/min, the surface areas were found to be 240, 98, and 87 m^2/g while the pore size distributions of 8, 10, and 16 nm, correspondingly, were obtained. On the other hand, CeO_2 materials were found to have very low BET surface areas of 1 m^2/g.

Thermal Stability Studies. Thermal stability of the as-synthesized γ-MnO_2 and CeO_2 materials was studied in a nitrogen atmosphere using thermogravimetric analyses (TGA) and differential scanning calorimetry (DSC). As shown in Figure 9, the weight of the CeO_2 materials decreased more rapidly between 30 and 200 °C as compared with that of γ-MnO_2 materials. However, between 200 and 500 °C, the weight of the γ-MnO_2 material decreased drastically to a low of about 82%. Unlike γ-MnO_2 results, CeO_2 materials showed a well-defined plateau at around 150−700 °C, followed by a dramatic increase in weight loss that is not observed for γ-MnO_2 samples. This plateau is similar to the one reported for CeO_2 nanocrystals.[27] In general, γ-MnO_2 materials showed a smaller overall weight loss (ca. 20%) as compared with that of CeO_2 materials (ca. 31%).
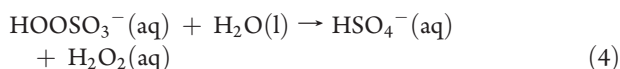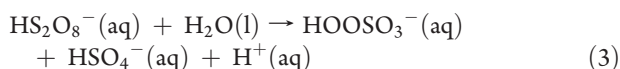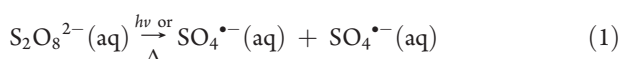
Catalytic Performance. γ-MnO_2 materials have recently been reported as potential tools of choice in the catalytic transformation of a wide range of organic substrates into more useful building blocks and/or end products. This is due to the excellent conversion and selectivity that these materials have shown in various catalytic systems.[10] Catalytic activities of the

as-synthesized γ-MnO$_2$ materials were tested for α-methyl styrene oxidation. The oxidation reactions were done three times for each catalyst, and results are summarized in Table 2. As shown in Table 2, γ-MnO$_2$ materials prepared at the lowest flow rate (1.0 mL/min) afforded a higher percent conversion (76%) compared with the γ-MnO$_2$ materials prepared at relatively higher flow rates (50%). In addition, selectivity toward acetophenone and α-methyl benzene acetaldehyde was higher with γ-MnO$_2$ materials prepared at 1.0 and 4.0 mL/min, respectively.
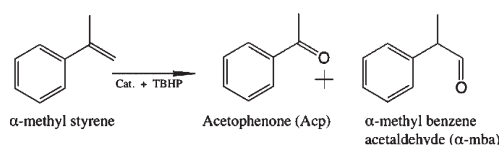
■ DISCUSSION

Persulfate Ion Decomposition and Metal Oxide Formation. Persulfate ions $(S_2O_8{}^{2-})$ have been used in the fabrication of a number of organic and inorganic materials. This is due to their high oxidizing power that stems from the cleavage of the peroxide bond $(^-O_3S-O-O-SO_3{}^-)$. Although these ions $(S_2O_8{}^{2-})$ have a strong oxidation potential $(E_o = 2.01$ V), on their own, they are kinetically slow to react with many inorganic and organic species since the peroxide bond requires energy to be cleaved for them $(S_2O_8{}^{2-})$ to react faster. To that effect, thermal energy, UV light, and even acids have, in the recent past, been used to energize and break this bond, thereby generating sulfate radicals $(SO_4{}^{\bullet-})$.[28] The sulfate radicals produced are stronger oxidants (2.5–3.1 V) than the persulfate ions;[29] therefore, they react with inorganic and organic species more rapidly to form the products of interest.

$S_2O_8{}^{2-}$ ions have been shown to decay asymmetrically and symmetrically through cleavage of O—S and O—O bonds in the presence of hydrogen ions (H^+)[30] and UV light,[31] respectively. Therefore, in our current study, $S_2O_8{}^{2-}$ decomposition is suggested to involve synergetic action of the UV light and the acid where photolysis proceeds as shown in eq 1,[28a,32] whereas acid-catalyzed decomposition of the $S_2O_8{}^{2-}$ ions proceeds as in eqs 2–5.[28a,33]

$$S_2O_8{}^{2-}(aq) \xrightarrow{h\nu \text{ or } \Delta} SO_4{}^{\bullet-}(aq) + SO_4{}^{\bullet-}(aq) \tag{1}$$

$$S_2O_8{}^{2-}(aq) + H^+(aq) \rightarrow HS_2O_8{}^-(aq) \tag{2}$$

$$HS_2O_8{}^-(aq) + H_2O(l) \rightarrow HOOSO_3{}^-(aq) + HSO_4{}^-(aq) + H^+(aq) \tag{3}$$

$$HOOSO_3{}^-(aq) + H_2O(l) \rightarrow HSO_4{}^-(aq) + H_2O_2(aq) \tag{4}$$

$$2H_2O_2(aq) \rightarrow 2H_2O(l) + O_2(g) \tag{5}$$
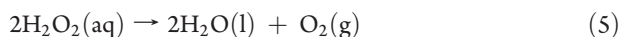
Thermal cleavage of the $S_2O_8{}^{2-}$ peroxide bond (O—O) has been utilized in an oil-bath or microwave heated reflux and hydrothermal syntheses of inorganic materials, such as OMS-2, CoOOH, and γ-MnO$_2$,[34] albeit in batch mode. In this mode (batch), the sluggish reactivity of the $S_2O_8{}^{2-}$ ions that arise from their slow decay is not a major concern since long reaction times are involved. However, in this work, microwave-promoted decay of $S_2O_8{}^{2-}$ ions could not afford continuous-flow synthesis of γ-MnO$_2$, OMS-2, and CeO$_2$ materials, as evidenced by the clear precursor solution obtained after microwave heating; see the Supporting Information, Figure S2a. This was attributed to the ineffectiveness of the microwave-supplied thermal energy in breaking $S_2O_8{}^{2-}$ peroxide bonds within the residence time offered

Table 2. Oxidation of α-Methyl Styrene with γ-MnO$_2$ and CeO$_2$ Catalysts[a]

α-methyl styrene → Cat. + TBHP → Acetophenone (Acp) + α-methyl benzene acetaldehyde (α-mba)

sample	S_{BET} (m^2 g^{-1})[b]	conversion (%)[c]	selectivity (%)[b]		
			Acp[d]	α-mba[e]	others
γ-MnO$_2$ (1 mL/min)	240	76(2)	76(2)	18(2)	6(2)
γ-MnO$_2$ (2 mL/min)	98	55(2)	78(2)	21(2)	3(4)
γ-MnO$_2$ (4 mL/min)	87	50(3)	26(3)	44(3)	30(4)
CeO$_2$ (1 mL/min)	1	18(3)	18(2)	78(2)	4(2)

[a] Reaction conditions: 1.0 mmol of α-methyl styrene, 2.0 mmol of TBHP, and 50 mg of catalyst were stirred in 10.0 mL of 1:9 ACN/DMF at 80 °C for 4 h. [b] Total surface area of a sample based on the BET method. [c] Product identified and quantified by GC-MS. [d] Acetophenone. [e] α-methyl benzene acetaldehyde. Experiments were done three times. Standard deviation given in parentheses.

by the 5 mL/min flow rate. Conversely, UV light $(\lambda = 253$ nm) afforded solid γ-MnO$_2$ and CeO$_2$ products (Figures 1 and 2).

The UV-light-stimulated rapid decomposition of the $S_2O_8{}^{2-}$ ions in the reaction mixture thereby generated very powerful oxidizing (2.5–3.1 V) sulfate radicals. The sulfate radicals oxidized Mn^{2+} and Ce^{3+} ions to the corresponding γ-MnO$_2$, CeO$_2$, and impure OMS-2 materials. This was ascribed to the lower redox potentials of the Mn^{2+}/Mn^{4+} and Ce^{3+}/Ce^{4+} ion pairs (1.28 and 1.44 V, respectively) compared to that of $SO_4{}^{\bullet-}$ ions.

The change in color of the precursor solutions from clear to light brown in the case of γ-MnO$_2$ materials or to light yellow for the CeO$_2$ materials (when the UV light was turned on) indicates the onset of nucleation triggered by the oxidation of the Mn^{2+} and Ce^{3+} ions by the sulfate radicals. As the precursor solutions together with the initial MnO$_2$ and CeO$_2$ nucleating species advanced through the coiled reactor and interacted more with the UV light, progressive oxidation of Mn^{2+} and Ce^{3+} ions into more nuclei and dissolution-recrystallization of these nuclei into small crystallites occurred. The transformation of the light brown or yellow solution to a dark brown or deep yellow suspension was, therefore, attributed to the formation of small MnO$_2$ and CeO$_2$ crystallites and their self-assembly into respective microspheres.

Effects of the Reaction Parameters on the Crystallization and Morphology of the γ-MnO$_2$ and CeO$_2$ Materials. *Flow Rate Effects and Drying Temperature.* From the continuous-flow catalysis standpoint, the rate of flow of the reactants/precursors has a direct impact on the reactant–catalyst interaction time (residence time) and hence the percent conversion realized. Likewise, in inorganic syntheses, flow rates significantly influence the crystallization and phase purity of the end materials. Recently, Opembe et al.[21] showed how flow rates influence reactant–microwave field interactions and hence the crystallization and purity of OMS-2 materials.

In our present study, the effects of flow rate and drying temperature on the crystallinity, purity, and morphology of the as-synthesized materials were investigated by FESEM and XRD

23279

dx.doi.org/10.1021/jp206942u |*J. Phys. Chem. C* 2011, 115, 23273–23282

studies. Drying temperature was found to have little or no effect on the crystallinity of the as-synthesized materials since no apparent changes in peak intensity and broadness was observed in materials dried at room temperature and at 120 °C; see the Supporting Information, Figure S3. Similarly, flow rates had no effect on the crystallinity and purity of the γ-MnO$_2$ materials (Figure 1) since neither extra (impurity) peaks nor obvious changes in crystallinity with the flow rate were observed. In contrast, OMS-2 materials, albeit with impurities, were only obtained at the lowest flow rate (1.0 mL/min); see Figure S4a (Supporting Information).

Therefore, the flow rates had little or no effect on the crystallization and the formation of the γ-MnO$_2$ phase but had profound effects on the evolution of the OMS-2 phase. This was attributed to the mixed 1 × 1, 1 × 2 and 1 × 1, 2 × 2 tunnel structure of the γ-MnO$_2$ and OMS-2 materials, respectively. On the basis of an in situ synchrotron X-ray diffraction work by Shen et al.,[35] disordered or layered precursors arising from MnO$_2$ nucleating species are reported to transform into 1 × 2 and mixed 1 × 1, 1 × 2 tunneled structures over time.[36] Therefore, the disordered MnO$_2$ precursor resulting from oxidization of Mn^{2+} ions by the sulfate radicals is suggested to have transformed into mixed 1 × 1, 1 × 2 and 2 × 2, 1 × 1 tunnel structures of γ-MnO$_2$ and OMS-2 materials, respectively, in our synthesis. In γ-MnO$_2$ materials, K$^+$ ions were not incorporated into the 1 × 1 and 1 × 2 tunnels to serve as counterions for charge balance, as is the case with the 2 × 2 tunnel structure of OMS-2 materials. As such, γ-MnO$_2$ materials formed readily at both the lowest and the highest flow rates.

Nonetheless, the transformation of the disordered MnO$_2$ precursor or layered structure to the 2 × 2, 1 × 1 tunnel structure of OMS-2 materials requires a relatively long residence time of 7.5—18 h[37] and the proper concentration of K$^+$ ions.[38] In addition, high temperature and/or pressure (which are not involved in the synthetic method presented herein) are also critical in the evolution of the OMS-2 tunnel structure.[39] The exclusive formation of the γ-MnO$_2$ materials at flow rates higher than 2.0 mL/min and the observation of the mixed OMS-2 and γ-MnO$_2$ phases at the lowest flow rate (1.0 mL/min) were thus attributed to the insufficient residence time for the disordered MnO$_2$ solid precursor to transform to the pure OMS-2 phase. On the other hand, the crystallinity of the CeO$_2$ materials decreased gradually with the increasing flow rate; see the (200) planes in Figure 2. This was due to the reduced crystal growth period arising from the reduced residence time. The broad XRD peaks observed for CeO$_2$ materials are indicative of the small CeO$_2$ crystallite size.

In addition to the crystallinity, the flow rate was found to have a significant impact on the morphology of the as-synthesized γ-MnO$_2$ and CeO$_2$ materials. At the lowest flow rate, 1.0 mL/min, the morphology of the materials consisted predominantly of well-formed microspheres; see panel (a) of Figures 3—5. On the other hand, poorly developed γ-MnO$_2$, and CeO$_2$ microspheres were formed at the highest flow rate; see Figures 3f, 4g, and 5e. Because no template or structure-directing agents were used, the γ-MnO$_2$ microspheres observed at low flow rates are suggested to arise from the self-assembly of the MnO$_2$ crystallites driven by the interfacial/surface forces involving the crystallites and the solvent employed.[18] CeO$_2$ microspheres, on the other hand, were probably formed by the self-assembly of the CeO$_2$ crystallites. Formation of well-formed γ-MnO$_2$ and CeO$_2$ microspheres at a low flow rate and poorly formed or no microspheres at a high flow rate is,

therefore, attributed to the relatively long and short residence times, respectively. Long residence periods gave the interfacial/surface forces ample time to assemble the MnO$_2$ and CeO$_2$ crystallites into γ-MnO$_2$ and CeO$_2$ microspheres.

Wavelength, pH, and Sulfate Ion (SO$_4^{2-}$) Concentration Effects. The synthetic protocol presented herein is largely dependent on the rapid decomposition of the persulfate ions effected by the UV light and acid, as opposed to the thermal energy supplied by either conventional or microwave heating. Because the cleavage of the S$_2$O$_8^{2-}$ peroxide bond requires energy, the generation of sulfate radicals and consequent formation of crystalline γ-MnO$_2$, CeO$_2$, and impure OMS-2 materials has a direct bearing on the energy associated with the light source used. Therefore, the formation of the light brown solution when 350 nm lamps were used instead of the dark brown suspension obtained with the 253 nm lamps and the failure of the clear precursor solution to change in color when visible lamps (λ = 700—400 nm) were used (see the Supporting Information, Figure S2b,c) was ascribed to the low energies associated with these relatively longer wavelengths (λ = 700—400, and 350 nm) as compared with that of the UV light, λ = 253 nm.

The effect of pH on morphology was tested in the pH range of 1—4, for both γ-MnO$_2$ and CeO$_2$ materials. The pH (through protonation and deprotonation surface groups) greatly influences the surface charge of nanoparticles and the interfacial interaction among them and with the solvent employed. Surface charge and interfacial forces have been found to be critical in self-assembly of nanoparticles,[18] determining colloidal stability, and construction of nanoarchitectures.[40] The formation of the agglomeration of γ-MnO$_2$ and CeO$_2$ materials in the absence of nitric acid (pH 3.88 and 3.67, respectively), as shown in Figures 3g, 5f, and 6a, is attributed to more van der Waals attractive and less electric repulsive forces between γ-MnO$_2$ and CeO$_2$ crystallites.

The isoelectric point, pH$_{IEP}$, of γ-MnO$_2$ and CeO$_2$ materials is about 4.5—5.0 and 4.43, respectively.[41] At these points, either γ-MnO$_2$ or CeO$_2$ particles are uncharged or the number of positive charges equals that of negative charges and thus interact more by van der Waals forces. At pH levels close to the pH$_{IEP}$ of these materials, such as pH 3.88 and 3.67 in our case, the particles associated more through van der Waals forces, and thus agglomeration occurred. However, when the pH was lowered below the pH$_{IEP}$, the respective crystallites (γ-MnO$_2$ and CeO$_2$) attained positive surface charges. Consequently, the electric repulsion increased and agglomeration decreased. To lower the surface energy of γ-MnO$_2$ and CeO$_2$ systems at low pH (1.10 and 1.90, in that order), the positive surface charge is smeared out[40] through the formation of spherical entities, which, in our case, are the γ-MnO$_2$ and CeO$_2$ microspheres (Figure 6a). The formation of γ-MnO$_2$ microspheres at high sulfate ion concentration as opposed to no microspheres at low concentration (Figure 6b) is partly attributed to the formation of small particles and large hexagonal nanoflakes. Small particles readily self-assemble under the influence of surface/interfacial forces than large particles. The understanding of the effect of sulfate ion concentration is currently being pursed in our continuing studies.

Fourier Transform Infrared and Inductively Coupled Plasma Optical Emission Spectrometry (ICP-OES). The FTIR spectra (spectra a and b) in Figure 7 for the γ-MnO$_2$ materials show absorption bands between 800 and 400 cm^{-1}, similar to the ones reported in the literature.[25] These absorption bands are ascribed to the Mn—O lattice vibrations of the MnO$_6$ octahedra

in the γ-MnO$_2$ framework. For the CeO$_2$ materials, spectrum c in Figure 7, the absorption bands between 800 and 400 cm^{-1} are attributed to the Ce—O lattice vibrations, while the broad intense band at 1250—950 cm^{-1} corresponds to the SO$_4^{2-}$ ions adsorbed on the Ce^{4+} surface cations of the CeO$_2$ materials, consistent with the work of Xu et al.[27]

The ICP-OES data (Table 1) of the representative γ-MnO$_2$ (prepared at pH 1.3 and a flow rate of 2.0 mL/min) and CeO$_2$ materials (prepared at 2.0 mL/min at varying pHs of 1.90, 1.79, 1.64, and 1.24) show no sulfur in the γ-MnO$_2$ samples. This implies that sulfur was neither incorporated in the structure of γ-MnO$_2$ materials nor adsorbed on the surface. On the other hand, consistent with the FTIR data (Figure 7) that show a broad intense band corresponding to sulfate ions adsorbed on the CeO$_2$ sample and no bands in the γ-MnO$_2$ materials, the amount of sulfur detected in the CeO$_2$ sample by the ICP-OES was substantial (56.24 mg/g on average). This is due to the strong adsorption of the sulfate ions on the surface of CeO$_2$ materials.[27]

N$_2$ Sorption Studies. The representative γ-MnO$_2$ materials exhibited type II and IV N$_2$ adsorption/desorption isotherms, quintessential for fibrous and globular systems, respectively.[42] The H$_2$-type hysteresis loop shown in Figure 8, curve c, confirms that the as-prepared γ-MnO$_2$ materials are porous materials with microspherical tertiary structures whose cavities are interconnected. This is in agreement with FESEM micrographs, Figure 4a,c,d, that show γ-MnO$_2$ with exposed cavities. On the other hand, the H$_3$-type hysteresis loop observed in the type II nitrogen adsorption/desorption isotherms of the γ-MnO$_2$ materials (Figure 8, curve a) is typical for slit-shaped mesopores of different sizes and shapes.[23a,b,43]

The adsorption isotherms in the P/P_0 range below 0.6 for both the γ-MnO$_2$ materials correspond to formation of monolayers and multilayers of adsorbate.[44] In the P/P_0 range below 0.6, the path followed by the adsorption isotherms of γ-MnO$_2$ materials is typical for micropore filling. This suggests the presence of microspores in these materials. At relative pressures P/P_o higher than 0.7, the rapid increase in the volume of the adsorbed molecules is attributed to the progressive filling of mesopores by capillary condensation.[11c,44] The high surface area (240 m^2/g) of the γ-MnO$_2$ materials synthesized at the lowest flow rate, as compared with the low surface area (87 m^2/g) obtained at the highest flow rate, was attributed to the high mesoporosity of these materials shown by the large hysteresis loop in Figure 8, curve c. This mesoporosity is suggested to arise from the well-developed microsphere morphology of the γ-MnO$_2$ materials (Figure 4a), and thus it is a contribution of the pores between adjoining microspheres, pores between nanofibers that construct the microspheres, and the pores due to the hollow cores (Figure 4c,d).

Thermal Stability and Catalytic Studies. Thermogravimetric analysis (TGA) studies (Figure 9) show the thermal stability of γ-MnO$_2$, and CeO$_2$ materials. The weight losses observed between 35 and 200 °C for γ-MnO$_2$ and CeO$_2$ materials were ascribed to the loss of the physisorbed water molecules on the surface of these materials.[9] Weight loss due to physisorbed water molecules has been observed at the same temperature range in manganese octahedral molecular sieves (OMS-2).[1c,23a,23b,37] The second weight loss (about 7%) occurring between 520 and 650 °C for γ-MnO$_2$ materials is attributed to the release of lattice oxygen consequent to the formation of Mn$_2$O$_3$.[9] On the other hand, the weight loss between 650 and 800 °C for the CeO$_2$ sample is suggested to arise from the decomposition of the

sulfate species adsorbed on these materials.[27] The TGA data, with respect to this weight loss, are in agreement with the FTIR spectra (Figure 7) that show sulfate species with an absorption band at 1250—950 cm^{-1} that is more intense in CeO$_2$ than in γ-MnO$_2$ materials. In addition, ICP-OES data are also in harmony with the TGA results since a relatively high amount of sulfur was detected in the CeO$_2$ systems and none in γ-MnO$_2$ materials.

The synthesized γ-MnO$_2$ materials showed good catalytic activity toward α-methyl styrene oxidation (Table 2). The higher percent conversion of the α-methyl styrene obtained with the γ-MnO$_2$ materials prepared at the lowest flow rate (1.0 mL/min) as compared with those synthesized at relatively higher flow rates (2.0 and 4.0 mL/min) is attributed to the high porosity (Figure 8, curve c) and surface area associated with the microsphere morphology of these materials. The γ-MnO$_2$ materials synthesized at the lowest flow rate were found to consist predominantly of well-formed microspheres (Figure 4a). The high porosity of the well-developed γ-MnO$_2$ microspheres is suggested to stem from pores between adjacent microspheres, pores between the nanofibers themselves, and the pores arising from the empty cores of the microspheres (Figure 4c,d). These pores allowed reactants an easy access to extra active sites within the γ-MnO$_2$ catalysts.

■ CONCLUSION

We have successfully demonstrated a continuous-flow, light-assisted synthesis of crystalline three-dimensional γ-MnO$_2$ materials with surface areas of 240, 98, and 87 m^2/g and CeO$_2$ microspheres with a BET surface area of 1 m^2/g. In contrast to the current continuous mode techniques that entail conventional or microwave heating, as well as the use of dielectric additives, such as ethylene glycol, to promote superheating, the present study establishes a new route by which crystalline metal oxide nanostructures can be prepared rapidly under nonthermal and atmospheric (pressure) conditions. As part of our continuing research, this technique is currently being extended to the preparation of ZnO and CoOOH.

■ ASSOCIATED CONTENT

ⓢ **Supporting Information.** Supporting data mentioned in the text, Figures S1—S8. This material is available free of charge via the Internet at http://pubs.acs.org.

■ AUTHOR INFORMATION

Corresponding Author
*E-mail: Steven.Suib@uconn.edu. Tel: 1 860 486 2797. Fax: 1 860 486 2981.

■ ACKNOWLEDGMENT

■ REFERENCES

(1) (a) Portehault, D.; Cassaignon, S.; Baudrin, E.; Jolivet, J.-P. *Cryst. Growth Des.* **2009**, *9*, 2562–2565. (b) Espinal, A. E.; Zhang, L.; Chen, C.-H.; Morey, A.; Nie, Y.; Espinal, L.; Wells, B. O.; Joesten, R.; Aindow, M.; Suib, S. L. *Nat. Mater.* **2010**, *9*, 55–59. (c) King'ondu, C. K.; Opembe, N.;

23281

dx.doi.org/10.1021/jp206942u |*J. Phys. Chem. C* 2011, 115, 23273–23282

Chen, C.-H.; Ngala, K.; Huang, H.; Iyer, A.; Garcés, H. F.; Suib, S. L. *Adv. Funct. Mater.* **2011**, *21*, 312–323. (d) Wang, Z. L.; Yin, J. S.; Jiang, Y. D. *Micron* **2000**, *31*, 571–580.

(2) Boaro, M.; Vicario, M.; Leitenburg, C.; Dolcetti, G.; Trovarelli, A. *Catal. Today* **2003**, *77*, 407–417.

(3) Yabe, S.; Yamashita, M.; Momose, S.; Tahira, K.; Yoshida, S.; Li, S.; Yin, S.; Sato, T. *Int. J. Inorg. Mater.* **2001**, *3*, 1003–1008.

(4) Masui, T.; Yamamoto, M.; Sakata, T.; Mori, H.; Adachi, G. *J. Mater. Chem.* **2000**, *10*, 353–357.

(5) Frangoul, A. G.; Sundaram, K. B.; Wahid, P. F. *J. Vac. Sci. Technol., B* **1991**, *9*, 181–183.

(6) Inaba, H.; Tagawa, H. *Solid State Ionics* **1996**, *83*, 1–16.

(7) Depner, S. W.; Kort, K, R.; Jaye, C.; Fischer, D. A.; Banerjee, S. *J. Phys. Chem. C* **2009**, *113*, 14126–14134.

(8) Jung, W. I.; Nagao, M.; Pitteloud, C.; Itoh, K.; Yamadaa, A.; Kanno, R. *J. Mater. Chem.* **2009**, *19*, 800–806.

(9) Xiaobo, F.; Jiyun, F.; Huan, W.; Ka Ming, N. *Catal. Commun.* **2009**, *10*, 1844–1848.

(10) Jin, L.; Chen, C.-H.; Crisostomo, V. M. B.; Xu, L.; Son, Y.-C.; Suib, S. L. *Appl. Catal., A* **2009**, *355*, 169–175.

(11) (a) De Wolff, P. M. *Acta Crystallogr.* **1959**, *12*, 341–345. (b) Chabre, Y.; Pannetier, J. *Prog. Solid State Chem.* **1995**, *23*, 1–130. (c) Benhaddad, L.; Makhloufi, L.; Messaoudi, B.; Rahmouni, K.; Takenouti, H. *ACS Appl. Mater. Interfaces* **2009**, *1*, 424–432.

(12) (a) Son, Y.-C.; Makwana, V. D.; Howell, A. R.; Suib, S. L. *Angew. Chem., Int. Ed.* **2001**, *40*, 4280–4283. (b) Makwana, V. D.; Son, Y.-C.; Howell, A. R.; Suib, S. L. *J. Catal.* **2002**, *210*, 46–52.

(13) Sithambaram, S.; Kumar, R.; Son, Y.-C.; Suib, S. L. *J. Catal.* **2008**, *253*, 269–277.

(14) (a) Iyer, A.; Galindo, H.; Sithambaram, S.; King'ondu, C.; Chen, C.-H.; Suib, S. L. *Appl. Catal., A* **2010**, *375*, 295–302. (b) Sriskandakumar, T.; Opembe, N.; Chen, C.-H.; Morey, A.; King'ondu, C.; Suib, S. L. *J. Phys. Chem. A* **2009**, *113*, 1523–1530. (c) Segal, S. R.; Suib, S. L. *Chem. Mater.* **1997**, *9*, 2526–2532.

(15) Masamichi, T. *Solvent Extr. Ion Exch.* **2001**, *19*, 531–551.

(16) (a) Zhou, K.; Yang, Z.; Yang, S. *Chem. Mater.* **2007**, *19*, 1215–1217. (b) Zhang, X. G.; Shen, C. M.; Li, H. L. *Mater. Res. Bull.* **2001**, *36*, 541–546. (c) Yuan, J.; Laubernds, K.; Villegas, J.; Gomez, S.; Suib, S. L. *Adv. Mater.* **2004**, *16*, 1729–1732.

(17) Guo, Z.; Du, F.; Li, G.; Cui, Z. *Cryst. Growth Des.* **2008**, *8*, 2674–2677.

(18) Yuan, J.; Laubernds, K.; Zhang, Q.; Suib, S. L. *J. Am. Chem. Soc.* **2003**, *125*, 4966–4967.

(19) King'ondu, C. K.; Iyer, A.; Njagi, E. C.; Opembe, N.; Genuino, H.; Huang, H.; Ristau, R. A.; Suib, S. L. *J. Am. Chem. Soc.* **2011**, *133*, 4186–4189.

(20) (a) Adschiri, T.; Hakuta, Y.; Sue, K.; Arai, K. *J. Nanopart. Res.* **2001**, *3*, 227–235. (b) Cabanas, A.; Poliakoff, M. *J. Mater. Chem.* **2001**, *11*, 1408–1416. (c) Takami, S.; Sato, T.; Mousavand, T.; Ohara, S.; Umetsu, M.; Adschiri, T. *Mater. Lett.* **2007**, *61*, 4769–4772. (d) Mousavand, T.; Ohara, S.; Umetsu, M.; Zhang, J.; Takami, S.; Naka, T.; Adschiri, T. *J. Supercrit. Fluids* **2007**, *40*, 397–401. (e) Sue, K.; Murata, K.; Kimura, K.; Arai, K. *Green Chem.* **2003**, *5*, 659–662. (f) Sue, K.; Hakuta, Y.; Smith, R. L.; Adschiri, T.; Arai, K. *J. Chem. Eng. Data* **1999**, *44*, 1422–1426. (g) Galkin, A. A.; Kostyuk, B. G.; Lunin, V. V.; Poliakoff, M. *Angew. Chem., Int. Ed.* **2000**, *39*, 2738–2740. (h) Choi, H.; Veriansyah, B.; Kim, J.; Kim, J.-D.; Kang, J. W. *J. Supercrit. Fluids* **2010**, *52*, 285–291.

(21) Opembe, N. N.; King'ondu, C. K.; Espinal, A. E.; Chen, C.-H.; Nyutu, E. K.; Crisostomo, V. M.; Suib, S. L. *J. Phys. Chem. C* **2010**, *114*, 14417–14426.

(22) (a) Behnajady, M. A.; Modirshahla, N.; Daneshvar, N.; Rabbani, M. *Chem. Eng. J.* **2007**, *127*, 167–176. (b) Behnajady, M. A.; Modirshahla, N.; Daneshvar, N.; Rabbani, M. *J. Hazard. Mater.* **2007**, *140*, 257–263.

(23) (a) Nyutu, E. K.; Chen, C.-H.; Sithambaram, S.; Crisostomo, V. M. B.; Suib, S. L. *J. Phys. Chem. C* **2008**, *112*, 6786–6793. (b) Malinger, K. A.; Ding, Y.-S.; Sithambaram, S.; Espinal, L.; Gomez, S.; Suib, S. L. *J. Catal.* **2006**, *239*, 290–298. (c) Huang, H.; Sithambaram, S.; Chen, C. H.;

King'ondu, C. K.; Xu, L.; Iyer, A.; Garces, H. F.; Suib, S. L. *Chem. Mater.* **2010**, *22*, 3664–3669.

(24) Huang, K.-C.; Couttenye, R. A.; Hoag, G. E. *Chemosphere* **2002**, *49*, 413–420.

(25) Ai, Z.; Zhang, L.; Kong, F.; Liu, H.; Xing, W.; Qiu, J. *Mater. Chem. Phys.* **2008**, *111*, 162–167.

(26) Ding, Y.-S.; Shen, X.-F.; Sithambaram, S.; Gomez, S.; Kumar, R.; Crisostomo, V. M. B.; Aindow, M.; Suib, S. L. *Chem. Mater.* **2005**, *17*, 5382–5389.

(27) Xu, J.; Li, G.; Li, L. *Mater. Res. Bull.* **2008**, *43*, 990–995.

(28) (a) Waldemer, R. H.; Tratnyek, P. G.; Johnson, R. L.; Nurmi, J. T. *Environ. Sci. Technol.* **2007**, *41*, 1010–1015. (b) Huang, K.-C.; Zhao, Z.; Hoag, G. E.; Dahmani, A.; Block, P. A. *Chemosphere* **2005**, *61*, 551–560. (c) Hayon, E.; McGarvey, J. J. *J. Phys. Chem.* **1967**, *71*, 1472–1477.

(29) (a) Liang, C.; Wang, Z.-S.; Bruell, C. J. *Chemosphere* **2007**, *66*, 106–113. (b) Liang, C.; Bruell, C. J.; Marley, M. C.; Sperry, K. L. *Chemosphere* **2004**, *55*, 1213–1223. (c) Watts, R. J.; Teel, A. L. *J. Environ. Eng.* **2005**, *131*, 612–622.

(30) Ye, Q.-F.; Wang, C.-Y.; Wang, D.-H.; Sun, G.; Xu, X.-H. *J. Zhejiang Univ., Sci., B* **2006**, *7*, 404–410.

(31) Criquet, J.; Karpel, V. L. N. *Chemosphere* **2009**, *77*, 194–200.

(32) (a) Ivanov, K. L.; Glebov, E. M.; Plyusnin, V. F.; Ivanov, Yu. V.; Grivin, V. P.; Bazhin, N. M. *J. Photochem. Photobiol., A* **2000**, *13*, 399–104. (b) Criquet, J.; Leitner, N. K. V. *Chemosphere* **2009**, *77*, 194–200.

(33) (a) Dogliotti, L.; Hayon, E. *J. Phys. Chem.* **1967**, *71*, 2511. (b) House, D. A. *Chem. Rev.* **1962**, *62*, 185.

(34) Chen, C.-H.; Abbas, S. F.; Morey, A.; Sithambaram, S.; Xu, L. P.; Garces, H. F.; Hines, W. A.; Suib, S. L. *Adv. Mater.* **2008**, *20*, 1205–1209.

(35) Shen, X.-F.; Ding, Y.-S.; Hanson, J. C.; Aindow, M.; Suib, S. L. *J. Am. Chem. Soc.* **2006**, *128*, 4570–4571.

(36) Portehault, D.; Cassaignon, S.; Baudrin, E.; Jolivet, J.-P. *Chem. Mater.* **2007**, *19*, 5410–5417.

(37) Villegas, J. C.; Garces, L. J.; Gomez, S.; Durand, J. P.; Suib, S. L. *Chem. Mater.* **2005**, *17*, 1910–1918.

(38) DeGuzman, R. N.; Shen, Y.-F.; Neth, E. J.; O'Young, C.-L.; Levine, S.; Newsam, J. M.; Suib, S. L. *Chem. Mater.* **1994**, *6*, 815–821.

(39) Huang, H.; Sithambaram, S.; Chen, C.-H.; King'ondu, C. K.; Xu, L.; Iyer, A.; Garces, H. F.; Suib, S. L. *Chem. Mater.* **2010**, *22*, 3664–3669.

(40) Abbas, Z.; Labbez, C.; Nordholm, S.; Ahlberg, E. *J. Phys. Chem. C* **2008**, *112*, 5715–5723.

(41) (a) Zhang, T. C.; Surampalli, R. Y.; Lai, K. C. K.; Hu, Z.; Tyagi, R. D.; Lo, I. M. C. *Nanotechnologies for Water Environment Applications*; American Society of Civil Engineers: Reston, VA, 2009; p 570. (b) Mao, J.; Bai, Y.; Gu, L.; van Aken, P. A.; Tu, M. *J. Nanopart. Res.* **2010**, *12*, 2045–2049.

(42) (a) Gregg, S. J.; Sing, K. S.W. *Adsorption, Surface Area and Porosity*, 2nd ed.; Academic Press: London, 1982; p 4. (b) Kolasinski, K. W. *Foundations of Catalysis and Nanoscience*, 2nd ed.; John Wiley and Son: West Sussex, England, 2008; p 236.

(43) Chen, X.; Shen, Y.-F.; O'Young, C. L.; Suib, S. L. *Chem. Mater.* **2002**, *14*, 940–948.

(44) Dias, A.; Ciminelli, V. S. T. *Ferroelectrics* **2000**, *241*, 9–16.